Research Square

Preprints are preliminary reports that have not undergone peer review.
They should not be considered conclusive, used to inform clinical practice,
or referenced by the media as validated information.

Source-Resolved PM2.5 Metals Emissions, Exposure, and Health Risks in California Using an Observation-Constrained Hybrid Model

Jie Zhang

jzhang9@lbl.gov

Lawrence Berkeley National Laboratory https://orcid.org/0000-0001-6400-3639

Ling Jin

ljin@lbl.gov

Lawrence Berkeley National Laboratory https://orcid.org/0000-0002-4381-195X

Research Article

Keywords:

Posted Date: November 3rd, 2026

DOI: https://doi.org/10.21203/rs.3.rs-11579816/v1

License: This work is licensed under a Creative Commons Attribution 4.0 International License.
Read Full License

Additional Declarations: The authors declare no competing interests.

Source-Resolved $PM_{2.5}$ Metals Emissions, Exposure, and Health Risks in California Using an Observation-Constrained Hybrid Model

Jie Zhang[1,*], Ling Jin[1,*], Qi Ying[2], Jia Xing[3], and Bin Wang[1]

1. Energy Analysis Division, Lawrence Berkeley National Laboratory, Berkeley, California 94720, United States
2. Division of Environment and Sustainability, The Hong Kong University of Science and Technology, Hong Kong, China
3. Department of Civil and Environmental Engineering, the University of Tennessee, Knoxville, Tennessee 37996, United States

* Correspondence: jzhang9@lbl.gov, ljin@lbl.gov

Abstract

Metals constitute a small fraction of $PM_{2.5}$ mass but can contribute disproportionately to its toxicity. Assessing their health risks requires spatially resolved estimates of individual metal concentrations and emission source contributions. However, sparse monitoring and uncertain source-specific metal profiles remain major barriers to such assessments. We developed an observation-constrained hybrid model integrating source-oriented chemical transport modeling and Bayesian inversion to constrain source-specific profiles and estimate emissions and population exposure for 23 $PM_{2.5}$ metals across 11 source sectors in California. The inversion improved modeling agreement with observations, reducing mean fractional errors from 0.835 to 0.511. For the noncarcinogenic effects, miscellaneous sources contributed 9.1% of emissions, 24.1% population-weighted exposure, and 57.7% of the hazard index, with Cd driving the hazard contribution. Industrial and miscellaneous sources each accounted for approximately 35% of excess lifetime cancer risk across six carcinogenic metals. Census-tract clusters characterized by substantial joint contributions from these sectors had the highest mean risks and were prominent in metropolitan Los Angeles. The framework provides observation-constrained source profiles and spatial exposure estimates for 23 metals, supporting epidemiological studies and community-level health assessments.

1. Introduction

Fine particulate matter ($PM_{2.5}$) is a leading environmental risk factor for premature mortality and morbidity worldwide, while long-term exposure has been consistently linked to cardiovascular, respiratory, and neurological diseases in epidemiological cohort studies.[1–3] Although metals typically constitute a minor fraction of total $PM_{2.5}$ mass, they contribute disproportionately to particle toxicity through mechanistically distinct biochemical pathways.[4–6] Airborne metals in $PM_{2.5}$ comprise a broad range of species, including crustal elements commonly associated with mineral dust (e.g., Fe, Al, Ti, Si) and trace elements often enriched by anthropogenic emissions at low atmospheric concentrations (e.g., Mn, Cu, V, Co, Ni). Their noncarcinogenic and carcinogenic effects vary with elemental identity, chemical form, and exposure level.[7,8] Consequently, assessing metal-related health risks requires consideration of both metal concentrations and their specific toxicities.

Metals such as Pb and Cd can disrupt essential ion transport, enzyme activity, and cellular signaling, with prolonged retention contributing to chronic noncarcinogenic effects.[9–12] Carcinogenic metals and metalloids act through overlapping genotoxic and epigenetic mechanisms, including oxidative DNA damage, inhibition of DNA repair, chromosomal instability, and epigenetic alterations.[13–17] International Agency for Research on Cancer (IARC) classifies As and its inorganic compounds, Cd and its compounds, Cr(VI) compounds, and Ni compounds as carcinogenic to humans (Group 1), whereas Co metal and soluble Co(II) salts are classified as probably carcinogenic to humans (Group 2A).[18–20]

Despite these well-established toxicological mechanisms, translating such knowledge into population-scale health risk estimates and advancing epidemiological research require spatially resolved metal concentration fields, which current monitoring infrastructure cannot adequately provide. In the United States, ambient $PM_{2.5}$ metal concentrations are primarily measured through the Environmental Protection Agency's (EPA) Chemical Speciation Network (CSN) and the Interagency Monitoring of Protected Visual Environments (IMPROVE) network. While these networks provide high-quality speciated observations, their sites remain spatially sparse, particularly relative to California's dense population and highly heterogeneous source landscape.[21] Consequently, relying solely on stationary monitors for exposure assessment is insufficient for resolving spatial gradients near localized emission sources, such as ports, industrial facilities, major transportation corridors, and dust-influenced regions. Moreover, even where measurements are available, the observational record typically provides total elemental mass concentrations without source attribution. This limitation leaves a critical gap in identifying which specific emission sectors drive the most toxicologically potent exposures.

Receptor models, such as positive matrix factorization (PMF), can infer source contributions from observed chemical compositions, but they are limited to specific monitoring locations and do not directly generate statewide exposure fields.[22,23] Chemical transport models (CTMs) provide spatially continuous concentration fields and can preserve links to specific emission sectors through source apportionment techniques. Yet, CTM-derived $PM_{2.5}$ metal predictions are highly sensitive to uncertainties in primary $PM_{2.5}$ emissions and source-specific metal speciation profiles. For airborne metals, this creates a methodological gap between the comprehensive spatial coverage

needed for population exposure assessments and the rigorous observational constraint necessary for metal-specific source attribution. Ultimately, this gap has implications for both health-risk interpretation and the design of targeted mitigation strategies, because source contributions to metal-attributable health risk may differ substantially.[24,25]

To address the gap, we developed an observation-constrained hybrid modeling framework to estimate source-resolved airborne metal exposure and their associated health risks across California. Building upon previous source-oriented hybrid air quality modeling efforts,[26,27] this study enhances that approach by applying a Bayesian inversion technique to constrain CTM predictions using surface measurements. The Bayesian framework preserves the spatial continuity and sectoral attribution of the CTM while utilizing surface observations to probabilistically update prior source-resolved metal fields. Unlike deterministic bias correction or empirical scaling, this approach explicitly accounts prior and observational uncertainties, constrains uncertain metal emissions and speciation profiles, and provides posterior concentration estimates for health-risk assessment.[28] The framework integrates source-resolved CTM simulations with monitoring data to generate high-resolution, spatially continuous concentration fields for 23 metals across 11 source sectors: Power, Industrial, Light-Duty Vehicle Exhaust (LDV_EXH), Heavy-Duty Vehicle Exhaust (HDV_EXH), Brake and Tire Wear, Off-road, Dust, Residential Wood Combustion (RWC), Miscellaneous, Fires, and Sea salt. We then quantified population-weighted exposures, noncarcinogenic hazard index, and excess lifetime cancer risks by metal and source sector. Clustering analysis identified census tracts typologies characterized by distinct patterns of joint contributions from multiple sources to health risks. This study tests whether sectors that dominate metal mass also dominate health risks, thereby identifying source categories and neighborhood types whose toxicological impacts are disproportionate to their emission contributions.

2. Methods

In this study, the framework combines sector-specific primary $PM_{2.5}$ ($PPM_{2.5}$) concentration fields from the Community Multiscale Air Quality (CMAQ) model simulations and prior source-specific metal speciation profiles. The resulting metal concentrations are constrained by surface measurements through Bayesian inference, as shown in Figure 1. The optimized posterior fields provide high-resolution regional $PM_{2.5}$ metal concentrations and source-apportioned contributions for subsequent analysis.

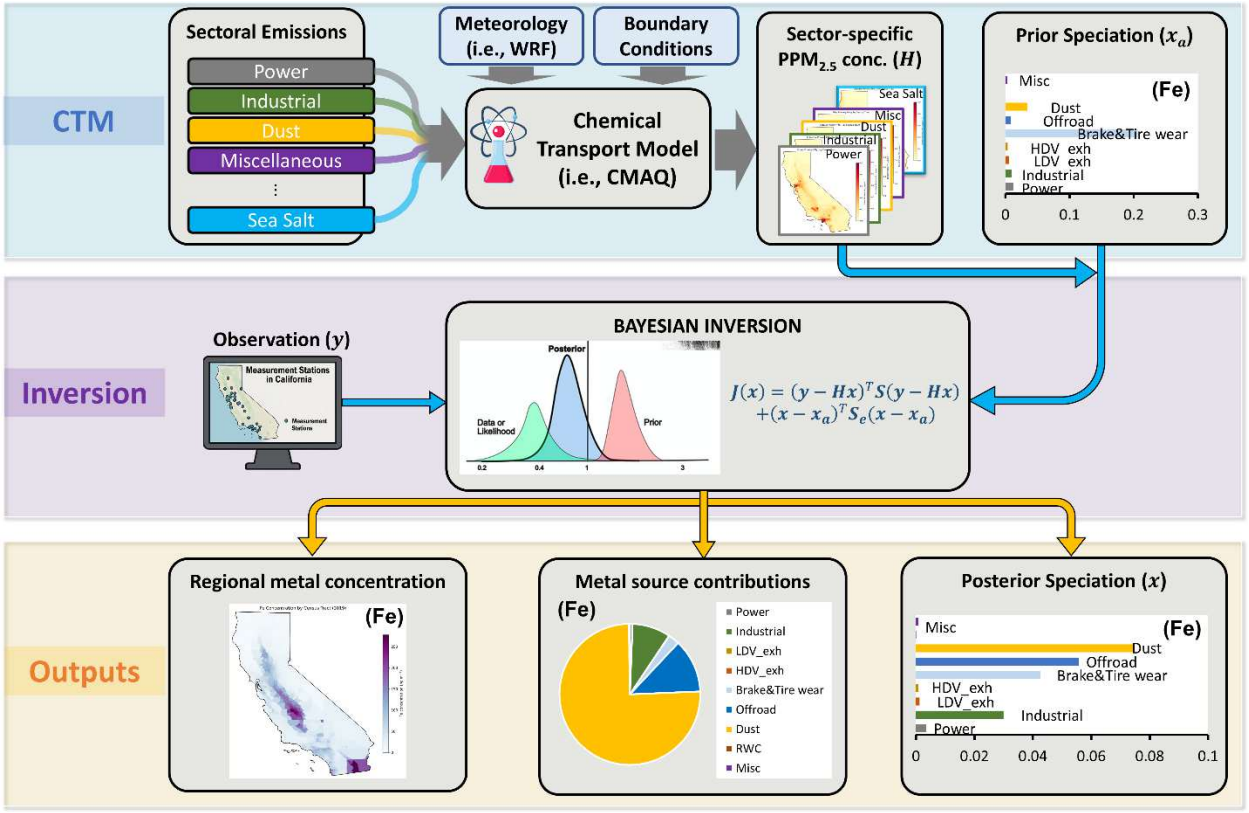


Figure 1. Schematic of the observation-constrained modeling framework for estimating source-resolved $PM_{2.5}$ metal concentrations.

2.1. $PM_{2.5}$ metal measurements and uncertainties

Daily $PM_{2.5}$ metal observations were obtained from US EPA Air Quality System (AQS) database, comprising measurements from 34 California monitoring sites in the IMPROVE and CSN networks (Figure S1). The dataset includes 23 $PM_{2.5}$ metal species analyzed via X-ray fluorescence-based methods: Method 800 for IMPROVE samples and Method 811 for CSN samples. These two methods share the same analytical basis but differ primarily in the sampler and filter size, which exert minor impacts on the measured concentrations. Therefore, no inter-method adjustment was applied to the dataset. In rare cases when both methods are collocated, the priority was given to IMPROVE-protocol. Metal- and method-specific observations were retained with their corresponding method detection limits (MDLs) and fractional uncertainties, as summarized in Table S1.[29,30]

Measurement-based uncertainties were estimated following the approach utilized in the EPA's Positive Matrix Factorization (PMF) model.[31] For a given metal m at a specific site i, method-specific MDLs and fractional uncertainties were assigned according to the corresponding AQS method code (Table S1). If the site-mean concentration ($\overline{C_{i,m}}$) was below or equal to the corresponding MDL, the site-specific observational uncertainty ($\sigma_{i,m}^{obs}$) was set to:

$$\sigma_{i,m}^{obs} = \frac{5}{6} MDL_{m,r} \quad (1)$$

If the site-mean concentration exceeded the MDL, the uncertainty was calculated as:

$$\sigma_{i,m}^{obs} = \sqrt{\left(u_{m,r}\overline{C_{\iota,m}}\right)^2 + \left(0.5MDL_{m,r}\right)^2} \quad (2)$$

where $u_{m,r}$ is the metal- and method-specific fractional uncertainty, and $MDL_{m,r}$ is the corresponding detection limit, and r denotes the AQS analytical method. This measurement uncertainty was then converted to log-space variance as:

$$var_{i,m} = \ln\left(1 + \left(\frac{\sigma_{i,m}^{obs}}{\overline{C_{\iota,m}}}\right)^2\right) \quad (3)$$

and used as the lower boundary for the site-specific variance of the model-observation error.

2.2. Sector-resolved $PM_{2.5}$ emission

Anthropogenic emissions were generated from California Air Resource Board's (CARB) emission inventories for the 2019 modeling year. For other than on-road emission sources, CARB's 2020 emission inventories were processed using the Sparse Matrix Operator Kernel Emissions (SMOKE) system to generate hourly, gridded, chemically speciated emissions. These emissions were then adjusted to 2019 levels using sector- and county-specific scaling factors derived from annual emission data reported by the California Emission Projection Analysis Model (CEPAM). On-road mobile emissions were generated directly from CARB's 2019 on-road inventory using the Emissions Spatial and Temporal Allocator (ESTA), providing detailed spatial and temporal representation of vehicle activity and emission patterns. In addition to these anthropogenic emissions, wind-blown dust and sea salt aerosols were generated dynamically using CMAQ inline modules.[32–34]

Total $PPM_{2.5}$ emissions were aggregated into 11 source sectors:

1) Power: area and point sources associated with fuel combustion for electricity generation.
2) Industrial: area and point source associated with petroleum production and industrial manufacturing.
3) LDV_EXH: tailpipe exhaust from on-road light-duty vehicles.
4) HDV_EXH: tailpipe exhaust from on-road heavy-duty vehicles.
5) Brake & Tire Wear: non-exhaust particles generated by brake and tire wear from all on-road vehicles.
6) Off-road: non-road mobile sources, including agricultural and construction equipment, aircraft, locomotives, and marine vessels.
7) Dust: fugitive dust from paved and unpaved roads, agricultural operations, and construction activities, together with natural windblown dust.
8) RWC: residential wood combustion.

9) Miscellaneous: other anthropogenic activities that not assigned to the other sectors, such as cooking, solvent use, surface coating, and waste disposal.
10) Fires: prescribed burning, agricultural burning, and accidental fires. Wildfires were excluded from this analysis, as there were few significant wildfire events in California during 2019 according the fire database.[35]
11) Sea salt: marine aerosol generated from sea spray.

These sector-resolved emissions were used to drive the source-tagged $PPM_{2.5}$ tracers in CMAQ. The resulting source-resolved $PPM_{2.5}$ concentration fields were then combined with source-specific metal speciation profiles to construct prior source-resolved metal concentration fields required by the Bayesian inversion framework. LDV_EXH, HDV_EXH, and Brake & Tire Wear were retained as separate source sectors in the emission processing and CTM simulations, however, their 4-km spatial concentration fields were highly correlated. Therefore, the three on-road sectors were combined during the Bayesian inversion to reduce collinearity, and their source-specific metal speciation profiles were scaled jointly by a common posterior factor.

2.3. Source-oriented $PM_{2.5}$ chemical transport model

Since $PM_{2.5}$ metals are emitted primarily as components of $PPM_{2.5}$, their spatial patterns depend heavily on the source locations of particle emissions, atmospheric transport, and removal processes. The regional source-oriented $PPM_{2.5}$ concentrations were simulated using the source-tagged tracer technique implemented in CMAQv5.5,[36] following our previous source-resolved modeling framework.[26–28] Briefly, sector-specific non-reactive $PPM_{2.5}$ tracers were added to the model aerosol species list and subjected to the same transport and removal processes as other chemical-inert particulate components. Tracer emissions were scaled by 10^{-5} to avoid perturbing particle size distributions or removal kinetics, and absolute sector-specific $PPM_{2.5}$ concentrations were recovered during postprocessing by applying a scaling factor of 10^5. This approach provides spatially continuous $PPM_{2.5}$ contributions from each source sector while maintaining consistency with modeled aerosol dynamics.

The CMAQ configuration followed our previous high-resolution California modeling work, where detailed descriptions of chemical mechanisms, meteorological inputs, boundary conditions, and model evaluation were reported.[28]

2.4. Prior $PM_{2.5}$ metal speciation profiles

Prior source-specific $PM_{2.5}$ metal speciation profiles were developed using two complementary approaches. For elements explicitly represented in CARB's speciation profiles, including Al, Ca, Fe, K, Mg, Mn, Na, Si, and Ti, sector-specific prior metal fractions were calculated directly from the emission inventory as the ratio of metal emissions to total $PPM_{2.5}$ emissions for each source sector:

$$\beta_{m,s}^{prior} = \frac{\sum_k E_{m,s}}{\sum_k E_{PPM_{2.5},s}} \quad (4)$$

where $E_{m,k}$ is the total prior emission of metal m from sector s, and $E_{PPM_{2.5},s}$ is the corresponding total $PPM_{2.5}$ emission from that sector.

For metals not included in CARB's original $PM_{2.5}$ speciation profiles, prior fractions were derived from EPA SPECIATE source-profile data originally compiled by Reff et al.[37] and mapped to the 11 source sectors used in this study. Source-profile metal mass fractions were determined using the 75th percentile of nonzero profile values. Median and geometric-mean aggregation were also evaluated, but the 75th-percentile statistic provided prior concentration estimates closer to observations. This selection is important because strongly biased priors could limit posterior adjustment in the Bayesian inversion, particularly for metal-sector combinations with limited observational constraints. The resulting prior metal speciation profiles are summarized in Table S2.

In addition to the 11 California source sectors, background metal concentrations were included to represent contributions transported into California from outside the modeling region or otherwise not attributable to in-state primary emissions. Background concentrations were derived from trace-metal measurements at the Point Reyes background monitoring site in California reported by Mastin et al.[38]

2.5. Log-space Bayesian Inversion Framework

We employed the log-space Bayesian inversion framework established by Zhang et al.[28] and adapted it here to estimate source-specific $PM_{2.5}$ metal speciation profiles. The inversion was applied independently for each metal species. For a given metal m, let n_m denote the number of observations and p denote the number of sectors, corresponding to 11 California source sectors plus the background term. Sector-resolved $PPM_{2.5}$ concentrations from CMAQ were assembled into the source-receptor matrix $\boldsymbol{K}_m \in \mathbb{R}^{n_m \times p}$, where each row corresponds to a specific observation and each column corresponds to a sector contribution. The observed concentration vector is $\boldsymbol{y}_m^{obs} \in \mathbb{R}^{n_m \times 1}$, and the unknown parameter vector is $\boldsymbol{\lambda}_m \in \mathbb{R}^{p \times 1}$, representing the sector-specific metal mass fractions for metal m. Prior estimates of $\boldsymbol{\lambda}_m^{prior}$ were provided as described above. In the forward model, $\boldsymbol{y}_m^{mod} = \boldsymbol{K}_m \boldsymbol{\lambda}_m$, is the modeled concentration vector paired with all observations. The inversion was performed in log space by defining $\boldsymbol{L}_m = \ln(\boldsymbol{\lambda}_m)$, ensuring positive posterior metal fractions and appropriately representing multiplicative uncertainties.[39]

The posterior estimates were obtained by minimizing the log-space Bayesian cost function:

$$J(\boldsymbol{L}_m) = [\ln(\boldsymbol{y}_m^{obs}) - \ln(\boldsymbol{K}_m e^{\boldsymbol{L_m}})]^T \boldsymbol{S}_{\boldsymbol{e,m}}^{-1} \left[\ln\left(\boldsymbol{y}_{\boldsymbol{m}}^{\boldsymbol{obs}}\right) - \ln(\boldsymbol{K_m} e^{\boldsymbol{L_m}})\right] + \left(\boldsymbol{L_m} - \boldsymbol{L}_{\boldsymbol{m}}^{\boldsymbol{prior}}\right) \boldsymbol{S}_{\boldsymbol{prior,m}}^{-1} \left(\boldsymbol{L_m} - \boldsymbol{L}_{\boldsymbol{m}}^{\boldsymbol{prior}}\right) \quad (5)$$

where $\boldsymbol{S_{e,m}} \in \mathbb{R}^{n_m \times n_m}$ is the observational error covariance matrix and $\boldsymbol{S_{prior,m}} \in \mathbb{R}^{p \times p}$ is the prior covariance matrix for the log-transformed metal fractions. The observation covariance matrix accounts for both measurement uncertainty and site-level model-observation mismatch. Measurement uncertainty was calculated from MDLs and fractional uncertainties using the PMF formulation (Eq. 1-3). The site-level residual variance was estimated from the log-space differences between prior model predictions and observations. For each site, the larger of these

two variance estimates was used for the diagonal elements in $\boldsymbol{S_{e,m}}$. For the off-diagonal elements, temporal covariance between observations at the same site was represented using an exponential decay function, whereas observations from different sites were assumed independent, as described in Zhang et al.[28]

The prior covariance matrix, $\boldsymbol{S_{prior,m}}$ was specified as a diagonal matrix representing uncertainty in the prior source-specific metal fractions. For each metal, the prior uncertainty for adjustable source sectors was assigned as a unit standard deviation in log space, corresponding to an e-fold multiplicative uncertainty in the prior speciation profile. This uncertainty accounts for variability among detailed source subcategories, uncertainty in source-profile data, sector-level aggregation, and potential mismatch between national source profiles and California-specific source composition. Fire and background terms were held constant at their prior values in the current implementation. The Maximum a Posteriori (MAP) and posterior uncertainties were derived from the posterior covariance matrix following Zhang et al.[28]

Following the metal-specific inversion, the optimized posterior source-resolved concentration fields ($C_{m,s}^{post}$) were calculated as:

$$C_{m,s}^{post} = H_s \cdot \lambda_{m,s}^{post} \quad (6)$$

where H_s is the CMAQ sector-resolved $PPM_{2.5}$ concentration for source sector s, and $\lambda_{m,s}^{post}$ is the optimized posterior mass fraction for metal m in sector s.

2.6. Health risk assessment

Health risks associated with optimized $PM_{2.5}$ metal concentrations were evaluated using standard noncarcinogenic and carcinogenic inhalation risk metrics following the methodology of EPA's Risk-Screening Environmental Indicators (RSEI) model.[40] For each metal m, the exposure concentration (EC_m) was calculated from the posterior annual mean concentration as:

$$EC_m = C_m^{post} \times \frac{ET \times EF \times ED}{AT} \quad (7)$$

where C_m^{post} is the posterior annual mean $PM_{2.5}$ metal concentration, ET is exposure time, EF is exposure frequency, ED is exposure duration, and AT is averaging time. For noncarcinogenic hazard, AT represents the averaging time over the exposure duration; for carcinogenic risk, AT represents lifetime averaging time. The reference value of parameters is listed in Table S3. Source-resolved EC_m were calculated analogously using $C_{m,s}^{post}$.

Noncarcinogenic effects were evaluated using hazard quotient (HQ) and hazard index (HI) metrics, which compare estimated exposure with chemical-specific reference concentrations, which are interpreted as screening-level indicators. For inhalation exposure, the HQ is the ratio of exposure concentration to the inhalation reference concentration (RfC_{inh}). The RfC_{inh} represents an estimate of continuous inhalation exposure expected to be without appreciable risk of adverse noncancer effects over a lifetime. For each metal m, the HQ_m was calculated as:

$$HQ_m = \frac{EC_m}{RfC_{inh}} \times 10^{-6} \quad (8)$$

where C_m^{post} is the posterior metal concentration in unit of ng m^{-3}, 10^{-6} converts ng m^{-3} to mg m^{-3}, and RfC_{inh} is reported in mg m^{-3} (Table S4). The cumulative hazard index for multiple metal pollutants was calculated as:

$$HI = \sum_m HQ_m \quad (9)$$

Source-resolved HQ and HI were calculated analogously using Eq. (8) and (9). An HQ or HI less than or equal to 1 indicates that adverse noncancer effects are not expected, whereas value greater than 1 indicate potential concern. Because HI assumes additivity across metals, it should be interpreted as a screening-level indicator of cumulative noncarcinogenic concern rather than a direct probability of adverse health effects.

Cancer risk was expressed as excess lifetime cancer risk (ELCR), which represents the incremental probability of developing cancer over a lifetime due to exposure to the carcinogenic pollutants. For metals with available inhalation unit risk (IUR) values (Table S4), $ELCR_m$ was calculated as:

$$ELCR_m = EC_m \times IUR_m \quad (10)$$

where EC_m is the exposure concentration of metal m, and IUR_m is the inhalation unit risk. Total cancer risk was calculated by summing across carcinogenic metals:

$$ELCR = \sum_m ELCR_m \quad (11)$$

2.7. Census-tract clustering analysis

To identify recurring spatial patterns in source-resolved metal exposure and risk, posterior gridded results were aggregated to California census tracts[41] using area-weighted polygon overlaps between 4-km CMAQ grid cells and tract boundaries. For each tract, source-specific risk contributions were normalized to fractional contributions so that clustering reflected relative source mixture rather than absolute risk magnitude. Census tracts were grouped using k-means clustering applied to the standardized source-risk fraction matrix. The number of clusters was selected manually using diagnostic metrics as references, including silhouette score and Davies-Bouldin index (DB index), together with interpretability of the resulting source profiles and spatial patterns. Mean source-risk fractions characterized the joint contributions of multiple sources within each cluster, and census tract cluster assignments were mapped to assess geographic coherence across California.

3. Results and Discussion

3.1. Observation-constrained model performance

The Bayesian inversion substantially improved agreement between modeled and observed site-specific annual-average $PM_{2.5}$ metal concentrations, as Figure 2. Across 23 metals at 34 California monitoring sites, the pooled mean fraction bias (MFB) improved from -0.689 to -0.223, while the mean fractional error (MFE) decreased from 0.835 to 0.511 (Table S5). The Pearson correlation (R) increased from 0.777 to 0.821. These improvements demonstrate that the observational constraints effectively corrected the systematic underprediction and overall prediction error in the prior estimates.

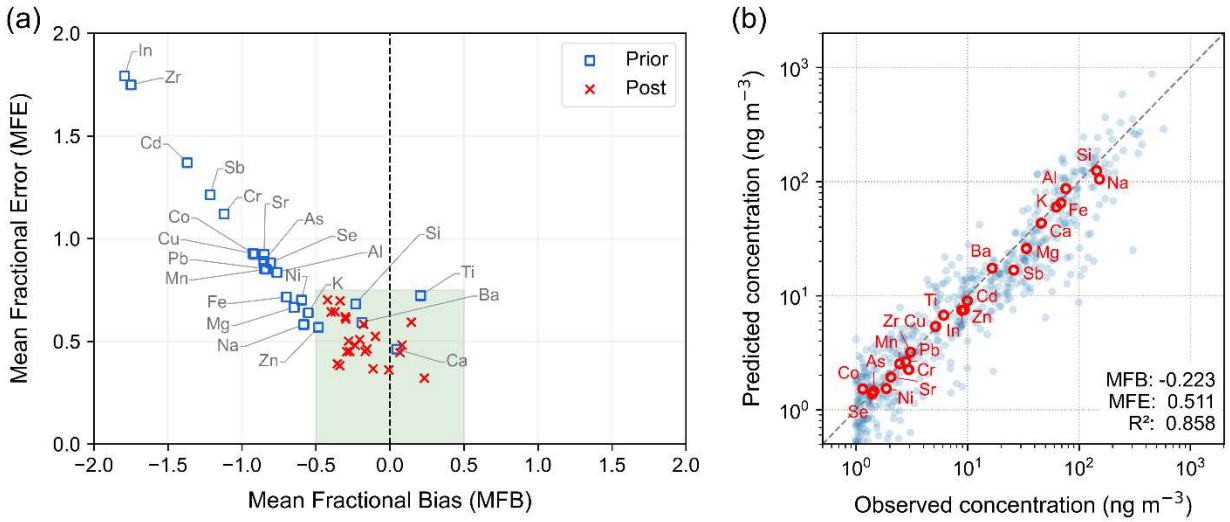


Figure 2. Performance of prior and posterior $PM_{2.5}$ metal concentration estimates. (a) MFB and MFE of site-specific annual-average concentrations for 23 metals. Blue squares and red crosses represent prior and posterior estimates, respectively. The shaded region denotes the criteria of -0.5 ⩽ MFB ⩽0.5 and MFE ⩽ 0.75. (b) Posterior vs. observed site-specific annual-average concentrations on logarithmic axes. Blue points represent individual metal-site pairs, and red circles represent the across-site mean concentrations for each metal. The dashed line indicates 1:1 agreement. Reported MFB, MFE, and R^2 are pooled across all metal-site pairs.

MFE decreased for 20 of the 23 metals (Table S5), indicating improvements across a broad range of species. Substantial reductions occurred for initially underpredicted metals such as Cd (1.370 to 0.451) and Cu (0.928 to 0.361). In contrast, MFE remained nearly unchanged for Ba (-0.190 to 0.144) and increased slightly for Ca (0.045 to -0.280) and Si (-0.232 to -0.421), whose prior estimates were close enough and the inversion did not further improve their agreement with observations. Daily log residuals, defined as $\ln(C_{post}/C_{prior})$, describe overprediction when positive and underprediction when negative. Log residuals are generally centered near zero across all 23 metals (Figure S2). This daily-scale assessment complements the improved annual-average agreement and provides further support for the posterior concentration estimates.

3.2. Posterior metal speciation profiles

Posterior metal speciation profiles exhibited distinct source signatures and are reported as estimates with uncertainty bounds in Table S6. The bounds were calculated as one standard

deviation (1σ) below and above the posterior estimate on the natural-log scale. The posterior dust profile was dominated by Si (18.2 [17.5-18.9]%) and Al (12.1 [11.6-12.5]%). This yields Si/Al mass ratio of 1.50, which is comparable with those measurements in urban fugitive dust from China (1.66-2.94). The posterior Ti/Al and Mn/Al mass ratios are 0.071 and 0.019, respectively, consistent with ranges of 0.06-0.12 and 0.02-0.03 measured in urban fugitive dust $PM_{2.5}$, supporting the crustal signature of the inferred profile.[42] The posterior sea salt fractions of Na (35.5 [33.9-37.1]%) and Mg (4.7 [44.3-49.7]%) slightly exceed the artificial inorganic sea-salt mixture values of 31% and 4%, respectively.[43] These fractions may overestimate those in natural sea-spray aerosols, where organic matter contributes additional particle mass.[44]

California's fossil-fuel power generation relies primarily on natural gas. The posterior power-sector mass fractions of Ca (0.34 [0.15-0.81]%), Al (0.59 [0.24-1.48]%), Ni (0.03 [0.01-0.07]%), and Zn (0.08 [0.03-0.19]%) are comparable to the values reported for gas-fired combined-cycle and cogeneration plants by England et al. (0.4%, 0.4%, 0.03%, and 0.1%, respectively).[45] Although posterior Pb and Co fractions are slightly higher than the reported values, but their 1σ uncertainty intervals encompassed the literature estimates. The posterior industrial profile contained substantial Fe (3.00 [2.54-5.33]%) and Al (2.20 [1.61-3.01]%), together with toxic trace metals including Cr, Ni, Cu, Zn, Cd, and Sb (Table S6). The mixed composition broadly resembles published industrial profiles, which commonly show abundant Fe and enrichment of multiple toxic metals.[46] However, reported metal fractions span wide ranges across industrial activities because of differences in raw materials, fuels, production processes, and emission controls.[26,27,47,48] This diversity introduces substantial uncertainty when representing industrial emissions with a single statewide profile. The posterior fractions therefore describe an effective aggregate composition, and may not capture the full variability among individual industrial sources.

The RWC posterior profile was dominated by K, accounting for 1.27 [1.13-1.43]% of emitted $PM_{2.5}$ (Table S6). This falls within the 0.46-2.74% range measured for wood-stove combustion of common US tree species.[48] The dominance of K and Zn (0.26 [0.24-0.29]%) is consistent with the experiments burning spruce and pine in a log-wood stove, where these are the two most abundant metallic elements in the emitted particles.[49] The miscellaneous sector combined diverse activities, including solvent and coating use, consumer products, asphalt paving and proofing, cooking, and waste disposal. Its posterior proof was characterized by Cd (0.5 [0.44-0.58]%) and Sb (0.44 [0.34-0.57]%) as the most abundant metals (Table S6). These fractions represent the aggregate composition of this heterogeneous sector.

The posterior off-road profile was dominated by Fe (5.58 [4.69-6.63]%), consistent with abundant Fe signature in construction-equipment exhaust (1.98-3.37%) and Fe-rich particles identified in agricultural-machine emissions (0.01-7.13%).[50,51] Ca, Mg, and Cu mass fractions fell within the measurement ranges in excavator exhaust.[52] The off-road category also includes marine vessels and aircraft, providing a plausible context for its higher Ni and Pb fractions relative to diesel-equipment measurements.[53,54] Ni occurs in marine-engine particles from heavy-oil combustion, whereas leaded aviation gasoline Pb-containing nanoparticles. These fuel-specific signatures may contribute to the posterior Ni (0.15 [0.12-0.19]%) and Pb (0.48 [0.38-0.60]%) fractions in the aggregated off-road profile (Table S6).

Posterior on-road exhaust profiles showed agreement with measured vehicle emissions for several metals (Table S7). The Ca fraction (0.30 [0.12-0.80]%) for LDV_EXH agreed with 0.37-0.40% reported for gasoline vehicles, while for HDV_EXH, Fe (0.074%) and Zn (0.038%) fell within reported diesel ranges of 0.03-0.58% and 0.03-0.77%, respectively.[55] Zn from HDV_EXH closely matched the fraction of 0.049% reported by Yang et al.[56], although in LDV_EXH, Zn was lower than gasoline measurements in both studies. Comparison with China heavy-duty diesel trucks further showed overlapping uncertainty intervals for Ca, Zn, Cu, and Pb, but lower posterior Fe and Al fractions, indicating variation among the diesel profiles compared.[50]

Table 1. Comparison of posterior brake & tire wear metal fractions with published $PM_{2.5}$ source profiles (%).

Metal	Posterior Brake & Tire Wear	Schauer et al. (2006) Brake Wear	Men et al. (2022) Brake wear	Schauer et al. (2006) Tire Wear
Fe	4.26 [3.03–5.99] [a]	2.69–49.88	16.6	0–0.134
Ba	2.94 [1.85–4.66]	0.479–2.137	-	0–0.013
Sb	0.154 [0.058–0.414]	0–0.471	-	0–0.001
Cu	0.099 [0.039–0.250]	0.020–1.628	-	0.003–0.017
Mn	0.098 [0.049–0.198]	0.012–0.375	0.126	0–0.002
Zn	0.097 [0.041-0.231]	0.030–1.075	-	0.021–0.335
Ti	0.075 [0.030–0.189]	0.008–0.623	-	0–0.004
Cr	0.022 [0.008–0.058]	0.006–0.052	0.059	0–0.007
Ni	0.020 [0.008–0.052]	-	0.008	-
Co	0.007 [0.003–0.020]	-	0.001	-

[a] Posterior estimates are followed by uncertainty bounds corresponding to ±1σ in log space, transformed back to the original scale.

Brake and tire wear metals have particular attention because elemental composition induces oxidative stress and inflammatory responses in human lung cells.[57–60] Their relative importance will increase as electrification reduces exhaust emissions, while greater vehicle mass may increase tire wear, although regenerative braking reduces brake wear.[61] The posterior brake & tire wear profile showed consistent with the reported source measurements[55], as Table 1, with Fe and Ba dominant and followed by Cu, Mn, Ti, Cr, and Zn. Posterior Mn (0.098[0.049-0.198]%) was comparable to the 0.126% measured in brake-dynamometer experiments.[62] Overall, our posterior profiles captured characteristic source-specific metal signatures. Overall, these observation-constrained profiles provide the basis for quantifying how individual emission sectors contribute to metal exposure and health risks.

3.3. Metal emissions, exposure, and health risks

Annual emissions of each metal were calculated by multiplying the sector-resolved primary $PM_{2.5}$ emissions by its corresponding posterior metal mass fraction and summing across sectors. Profile uncertainties were propagated through 100,000 Monte Carlo simulations, independently sampling metal-source fractions from log-normal distributions defined by their posterior estimates and log-scale standard deviations (σ). Emissions are reported as medians and 95% uncertainty intervals in

Figure S3. The emissions included anthropogenic fugitive dust but excluded natural sea salt and windblown dust. Si has the highest annual emissions at 8.93 [8.27-9.71] kt yr^{-1}, followed by Al at 6.01 [5.58-6.51] kt yr^{-1} and Fe at 4.60 [4.25-5.00] kt yr^{-1}. Together with K, Na, Ca, and Mg, these crustal elements accounted for approximately 90% of the estimated metal emission mass, which are mainly emitted from anthropogenic fugitive dust due to human activities.[37] The 11 metals evaluated for health risks collectively contribute 2.05 [1.90-2.22] kt yr^{-1}, approximately 5.8% of total metal emissions. Individual metal emission maps showed broadly similar spatial patterns, with elevated emission from Los Angeles, San Francisco Bay Area, Imperial Valley, and Central Valley (Figure S4).

Annual-average metal concentrations were calculated by multiplying the modeled sector-resolved primary $PM_{2.5}$ concentrations by the corresponding posterior metal mass fractions and summing across sectors. For urban-rural comparisons, the metal concentrations were first aggregated to census tracts using grid-tract overlap areas as weights, as described in Section 2.7. Census tracts were classified using the 2010 Rural-Urban Commuting Area (RUCA) codes, which characterize population density, urbanization, and commuting patterns.[63] For this study, primary codes 1-3 (metropolitan areas) were grouped as urban, and codes 4-10 (micropolitan, small-town, and rural areas) as rural (Figure S5). Na has the highest concentrations in both urban and rural areas, followed by Si, Al, and Fe. Urban metal concentrations exceeded rural values for all 23 metals by factors of 1.87-4.27 (Figure S6). The contrasts were particularly pronounced for toxic metals such as Cd (4.27), Pb (3.15), and Cu (2.99), indicating stronger urban enrichment than for abundant elements such as Na and Si. Individual metal concentration maps showed elevated concentrations across the Central Valley, the Los Angeles metropolitan area, and the Imperial Valley, while Na also exhibited pronounced coastal enhancements consistent with sea-salt contributions (Figure S7).

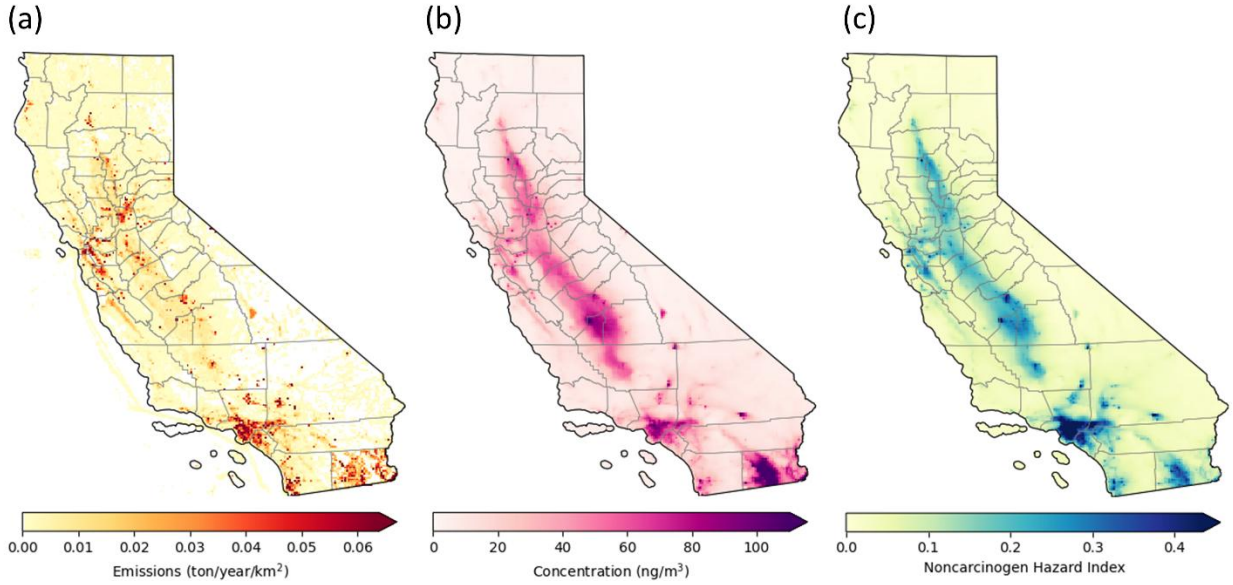


Figure 3. Spatial distribution of (a) annual anthropogenic emission (ton yr^{-1} km^{-2}), (b) annual-average ambient concentration (ng m^{-3}), and (c) noncarcinogenic HI for 11 $PM_{2.5}$ metals, including As, Cd, Co, Cr, Cu, Mn, Ni, Pb, Sb, Se, and Zn.

Emissions of the 11 metals assessed for noncarcinogenic impacts showed localized hotspots in the Los Angeles metropolitan area, San Francisco Bay Area, Central Valley, and the dessert area in Imperial Valley (Figure 3a), while their combined concentrations exhibited broader regional enhancements, particularly across the Central Valley and southern California (Figure 3b). Accounting for metal-specific inhalation toxicity (Section 2.6) highlighted the Los Angeles metropolitan area as a major hotspot of the noncarcinogenic HI as Figure 3c. Cd and As contribute strongly to HI because their low RfC_{inh} values (Table S4) result in greater HQ per unit concentration than those of Zn and Cu. The HI across California has a median of 0.034 and 95th-percentile HI of 0.208, which is comparable with the reported values in previous studies for other cities.[64,65] Therefore, the spatial distribution of noncarcinogenic hazard reflects the combined effects of emission patterns, atmospheric transport, and the composition and toxicity of airborne metals.

The six metals evaluated for cancer risks exhibited similar emission and concentration patterns, with regional enhancements across the Central Valley and southern California (Figure S8). Among these carcinogenic metals, airborne Cr exists primarily as Cr(III) and Cr(VI), with Cr(VI) serving as the basis for Cr inhalation cancer-risk assessment.[66] Because our inversion estimated total Cr without distinguishing oxidation state, Cr(VI) concentrations were calculated by multiplying source-specific ratio of Cr(VI)/total-Cr. The ratios were selected from published modeling defaults[67,68], California risk assessments[69], and ambient Cr measurements[70], with surrogate values explicitly identified where direct source measurements were unavailable (Table S8). The resulting Cr(VI) concentrations were used to assess Cr-related cancer risk. Under the specific 70-year lifetime exposure scenario, the median and 95th-percential ELCR across California are 1.72×10^{-6} and 1.03×10^{-5}, respectively. Localized ELCRs exceeded 10^{-5}, corresponding to an estimated excess lifetime cancer cases greater than 10 in one million, which is a typical cancer risk management benchmark.[71]

3.4. Source contributions to metal emission, exposure, and health risks

Source contributions to population-weighted exposure substantially differs from their emissions as Figure 4. Miscellaneous sector accounted for 9.1% of noncarcinogenic toxic metal emissions but 24.1% of exposure, with a similar increase from 16.1% to 37.4% for carcinogenic metals. Conversely, dust exposure shares were approximately half its emission shares. The increased importance of miscellaneous sources is because this sector contains residential and urban activities whose emissions occur close to populated areas. Industrial sector accounted for 29.5% and 28.7% of emissions of noncarcinogenic and carcinogenic metals, respectively, and remained a major contributor to exposure at 27.1% and 23.1%.

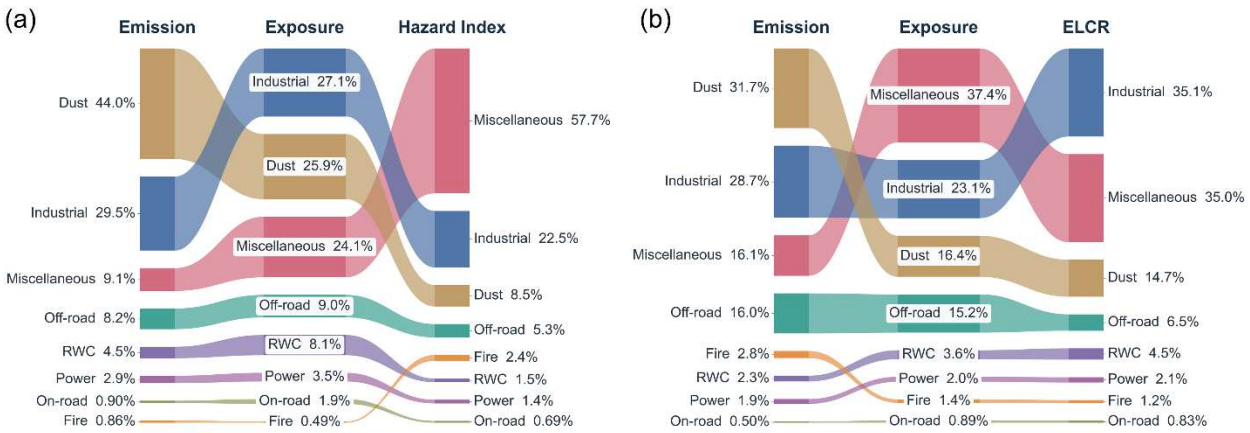


Figure 4. Source contributions to annual metal emissions, population-weighted exposure, and associated health risks in California: (a) noncarcinogenic metals and (b) carcinogenic metals. On-road sector combines LDV_EXH, HDV_EXH, and Brake & Tire Wear.

Toxicity weighting further increased the importance of miscellaneous sources, which contributed 57.7% of HI, followed by industrial at 22.5% (Figure 4a). This pattern largely reflected Cd, which accounted for 74.0% of HI despite representing only 12.1% of population-weighted exposure (Figure S9). The large contribution of miscellaneous sources to Cd exposure, combined with Cd's high inhalation toxicity, drove this sector's substantial contribution to HI. Industrial sector contributed 22.5% of HI, driven primarily by Cd and As. Dust accounted for 25.9% of metal exposure but only 8.5% of HI, reflecting a greater proportion of metals with lower inhalation toxicity (e.g., Zn and Cu), compared with industrial and miscellaneous sources.

Cancer risk was shared more evenly between industrial and miscellaneous sources, which contributed 35.1% and 35.0% of ELCR, respectively (Figure 4b). Their contributions reflected different metal compositions: Cr(VI) dominated industrial ELCR, whereas Cd dominated miscellaneous ELCR. Compared with the strong Cd dominance in noncarcinogenic hazard, cancer risk was distributed more broadly among Cd (34.8%), Co (24.3%), Cr(VI) (24.2%), and As (15.2%) (Figure S10). These source contributions describe the metals and health endpoints represented by the reference concentrations and inhalation unit risks. They do not quantify the full toxicity of traffic-related particles, including the oxidative effects of Fe-rich wear particles discussed above.

To identify how the sources jointly driving health risks varied among communities, census tracts were clustered according to their relative source contributions to HI and ELCR. After evaluating cluster numbers, 5 HI clusters and 6 ELCR clusters were selected manually, guided by silhouette scores, the DB index, and source-profile interpretability, while avoiding redundant or scientifically uninformative subdivisions (Figure S11). For noncarcinogenic HI, calculated as sum of HQs for all 11 assessed metals, the largest cluster comprised 4,040 tracts (50.3%) and was dominated in the Los Angeles metropolitan area. This cluster combined dominant miscellaneous contributions with substantial industrial contributions and had a mean HI of 0.39, compared with 0.16-0.17 in the other clusters (Figure S12).

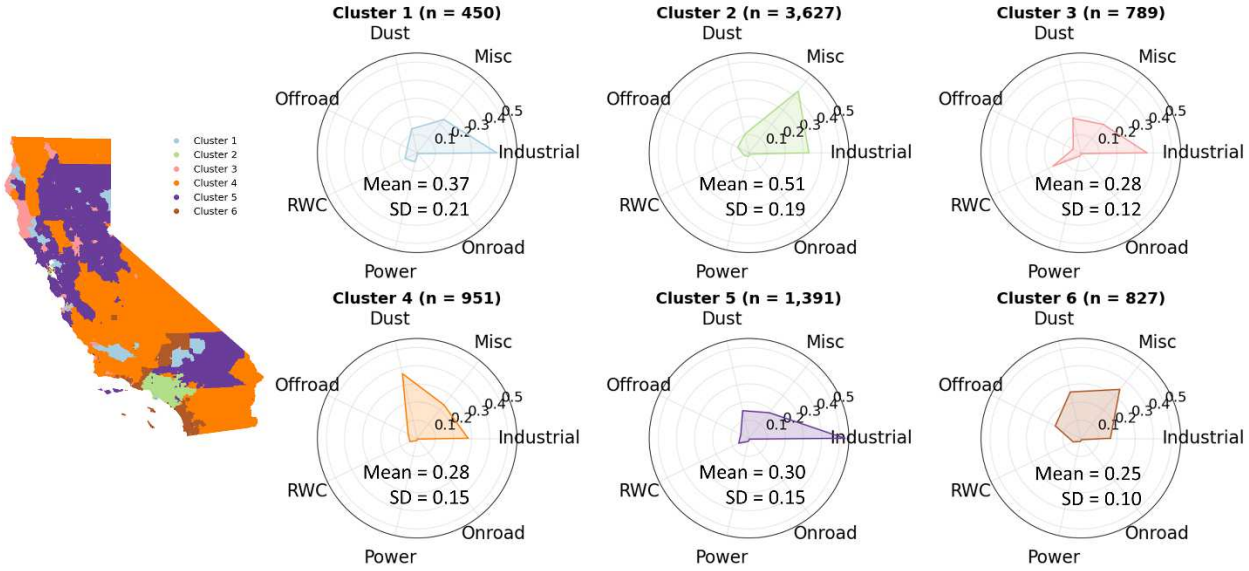


Figure 5. Spatial distribution and source-risk profiles of six census-tract clusters characterized by joint source contributions to ELCR in California. Map colors indicate cluster membership, and radar charts show mean source-specific fractions of ELCR within each cluster. *n* denotes the number of census tracts. Mean and SD summarize tract-level ELCR within each cluster and are expressed in units of 10^{-5}.

Cancer-risk clustering revealed distinct regional source mixtures underlying the statewide industrial and miscellaneous contributions (Figure 5). Cluster 2 comprised 3,627 tracts (45.1%) and was prominent in the Los Angeles metropolitan area, with substantial contributions from both miscellaneous and industrial sources. This cluster had the highest mean ELCR of 5.1×10^{-6}, consistent with the combined influence of Cd-rich miscellaneous sources and industrial sector containing Cr(VI) and As, which contribute strongly to cancer risk because of their high IUR. Industrial-dominated Cluster 1 and 5 had lower mean ELCRs of 3.7×10^{-6} and 3.0×10^{-6}, respectively, despite the stronger industrial dominance in Cluster 5. Clusters with greater RWC influence (Cluster 3), dust contributions (Cluster 4), or a more balanced source mixture (Cluster 6) had lower mean ELCRs of 2.5-2.8×10^{-6}. Within-cluster distributions further revealed differences obscured by these averages: Cluster 1 exhibited a broad, bimodal distribution, indicating that communities with similar relative source contributions could experience substantially different risk levels (Figure S13).

This study integrated surface observations with source-oriented modeling to link $PM_{2.5}$-metal emissions, population exposure, and health risks across California. The results identified substantial contributions from miscellaneous and industrial sources to health risks, while census-tract clustering revealed distinct community-level source joint contributions underlying the statewide averages. Because this framework relies on observations to constrain source-specific metal profiles, sparse monitoring coverage and uneven data availability across metals limit these constraints, while the limited range of routinely monitored trace metals restricts the scope of the assessment. Additional monitoring coverage and measurements of trace metals could strengthen

the observation constraints on source-specific profiles. The posterior $PM_{2.5}$ metal speciation profiles developed here provide inputs for constructing sector-resolved metal emission inventories, supporting atmospheric transport, deposition, and chemical-process studies. The concentration fields can be linked to residential health records to investigate associations between health outcomes and exposure to individual metals or joint contributions for further epidemiological investigations.

References

(1) Li, T.; Zhang, Y.; Wang, J.; Xu, D.; Yin, Z.; Chen, H.; Lv, Y.; Luo, J.; Zeng, Y.; Liu, Y.; Kinney, P. L.; Shi, X. All-Cause Mortality Risk Associated with Long-Term Exposure to Ambient PM2·5 in China: A Cohort Study. *The Lancet Public Health* **2018**, *3* (10), e470–e477. https://doi.org/10.1016/S2468-2667(18)30144-0

(2) Liu, Q.; Xu, C.; Ji, G.; Liu, H.; Shao, W.; Zhang, C.; Gu, A.; Zhao, P. Effect of Exposure to Ambient PM2.5 Pollution on the Risk of Respiratory Tract Diseases: A Meta-Analysis of Cohort Studies. *J Biomed Res* **2017**, *31* (2), 130–142. https://doi.org/10.7555/JBR.31.20160071

(3) Shi, L.; Wu, X.; Yazdi, M. D.; Braun, D.; Awad, Y. A.; Wei, Y.; Liu, P.; Di, Q.; Wang, Y.; Schwartz, J.; Dominici, F.; Kioumourtzoglou, M.-A.; Zanobetti, A. Long-Term Effects of PM2·5 on Neurological Disorders in the American Medicare Population: A Longitudinal Cohort Study. *The Lancet Planetary Health* **2020**, *4* (12), e557–e565. https://doi.org/10.1016/S2542-5196(20)30227-8

(4) Maciejczyk, P.; Chen, L.-C.; Thurston, G. The Role of Fossil Fuel Combustion Metals in PM2.5 Air Pollution Health Associations. *Atmosphere* **2021**, *12* (9). https://doi.org/10.3390/atmos12091086

(5) Chen, Y.; Luo, X.-S.; Zhao, Z.; Chen, Q.; Wu, D.; Sun, X.; Wu, L.; Jin, L. Summer–Winter Differences of PM2.5 Toxicity to Human Alveolar Epithelial Cells (A549) and the Roles of Transition Metals. *Ecotoxicology and Environmental Safety* **2018**, *165*, 505–509. https://doi.org/10.1016/j.ecoenv.2018.09.034

(6) Guo, F.; Tang, M.; Wang, X.; Yu, Z.; Wei, F.; Zhang, X.; Jin, M.; Wang, J.; Xu, D.; Chen, Z.; Chen, K. Characteristics, Sources, and Health Risks of Trace Metals in PM2.5. *Atmospheric Environment* **2022**, *289*, 119314. https://doi.org/10.1016/j.atmosenv.2022.119314

(7) Jomova, K.; Alomar, S. Y.; Nepovimova, E.; Kuca, K.; Valko, M. Heavy Metals: Toxicity and Human Health Effects. *Arch Toxicol* **2025**, *99* (1), 153–209. https://doi.org/10.1007/s00204-024-03903-2

(8) Jaishankar, M.; Tseten, T.; Anbalagan, N.; Mathew, B. B.; Beeregowda, K. N. Toxicity, Mechanism and Health Effects of Some Heavy Metals. *Interdiscip Toxicol* **2014**, *7* (2), 60–72. https://doi.org/10.2478/intox-2014-0009

(9) Bridges, C. C.; Zalups, R. K. Molecular and Ionic Mimicry and the Transport of Toxic Metals. *Toxicology and Applied Pharmacology* **2005**, *204* (3), 274–308. https://doi.org/10.1016/j.taap.2004.09.007

(10) Vesey, D. A. Transport Pathways for Cadmium in the Intestine and Kidney Proximal Tubule: Focus on the Interaction with Essential Metals. *Toxicology Letters* **2010**, *198* (1), 13–19. https://doi.org/10.1016/j.toxlet.2010.05.004

(11) Yang, H.; Shu, Y. Cadmium Transporters in the Kidney and Cadmium-Induced Nephrotoxicity. *International Journal of Molecular Sciences* **2015**, *16* (1), 1484–1494. https://doi.org/10.3390/ijms16011484
(12) Godwin, H. A. The Biological Chemistry of Lead. *Current Opinion in Chemical Biology* **2001**, *5* (2), 223–227. https://doi.org/10.1016/S1367-5931(00)00194-0
(13) Balali-Mood, M.; Naseri, K.; Tahergorabi, Z.; Khazdair, M. R.; Sadeghi, M. Toxic Mechanisms of Five Heavy Metals: Mercury, Lead, Chromium, Cadmium, and Arsenic. *Front. Pharmacol.* **2021**, *12*. https://doi.org/10.3389/fphar.2021.643972
(14) Zhu, Y.; Costa, M. Metals and Molecular Carcinogenesis. *Carcinogenesis* **2020**, *41* (9), 1161–1172. https://doi.org/10.1093/carcin/bgaa076
(15) Zhao, L.; Islam, R.; Wang, Y.; Zhang, X.; Liu, L.-Z. Epigenetic Regulation in Chromium-, Nickel- and Cadmium-Induced Carcinogenesis. *Cancers* **2022**, *14* (23). https://doi.org/10.3390/cancers14235768
(16) Tam, L. M.; Price, N. E.; Wang, Y. Molecular Mechanisms of Arsenic-Induced Disruption of DNA Repair. *Chem. Res. Toxicol.* **2020**, *33* (3), 709–726. https://doi.org/10.1021/acs.chemrestox.9b00464
(17) Zhitkovich, A. Chromium in Drinking Water: Sources, Metabolism, and Cancer Risks. *Chem. Res. Toxicol.* **2011**, *24* (10), 1617–1629. https://doi.org/10.1021/tx200251t
(18) IARC. *Arsenic, Metals, Fibres, and Dusts*.
(19) International Agency for Research on Cancer. *Arsenic, Metals, Fibres, and Dusts*; IARC Monographs on the Evaluation of Carcinogenic Risks to Humans; International Agency for Research on Cancer: Lyon, France, 2012; Vol. 100C.
(20) International Agency for Research on Cancer. *Cobalt, Antimony Compounds, and Weapons-Grade Tungsten Alloy*; IARC Monographs on the Identification of Carcinogenic Hazards to Humans; International Agency for Research on Cancer: Lyon, France, 2023; Vol. 131.
(21) Solomon, P. A.; Crumpler, D.; Flanagan, J. B.; Jayanty, R. K. M.; Rickman, E. E.; McDade, C. E. U.S. National PM2.5 Chemical Speciation Monitoring Networks—CSN and IMPROVE: Description of Networks. *Journal of the Air & Waste Management Association* **2014**, *64* (12), 1410–1438. https://doi.org/10.1080/10962247.2014.956904
(22) Paatero, P.; Tapper, U. Positive Matrix Factorization: A Non-Negative Factor Model with Optimal Utilization of Error Estimates of Data Values. *Environmetrics* **1994**, *5* (2), 111–126. https://doi.org/10.1002/env.3170050203
(23) Mousavi, A.; Sowlat, M. H.; Sioutas, C. Diurnal and Seasonal Trends and Source Apportionment of Redox-Active Metals in Los Angeles Using a Novel Online Metal Monitor and Positive Matrix Factorization (PMF). *Atmospheric Environment* **2018**, *174*, 15–24. https://doi.org/10.1016/j.atmosenv.2017.11.034
(24) Xie, J.; Jin, L.; Cui, J.; Luo, X.; Li, J.; Zhang, G.; Li, X. Health Risk-Oriented Source Apportionment of PM2.5-Associated Trace Metals. *Environmental Pollution* **2020**, *262*, 114655. https://doi.org/10.1016/j.envpol.2020.114655
(25) Liu, J.; Chen, Y.; Chao, S.; Cao, H.; Zhang, A.; Yang, Y. Emission Control Priority of PM2.5-Bound Heavy Metals in Different Seasons: A Comprehensive Analysis from Health Risk Perspective. *Science of The Total Environment* **2018**, *644*, 20–30. https://doi.org/10.1016/j.scitotenv.2018.06.226
(26) Ying, Q.; Feng, M.; Song, D.; Wu, L.; Hu, J.; Zhang, H.; Kleeman, M. J.; Li, X. Improve Regional Distribution and Source Apportionment of PM2.5 Trace Elements in China Using

Inventory-Observation Constrained Emission Factors. *Science of The Total Environment* **2018**, *624*, 355–365. https://doi.org/10.1016/j.scitotenv.2017.12.138
(27) Liao, K.; Zhang, J.; Chen, Y.; Lu, X.; Fung, J. C. H.; Ying, Q.; Yu, J. Z. Regional Source Apportionment of Trace Metals in Fine Particulate Matter Using an Observation-Constrained Hybrid Model. *npj Clim Atmos Sci* **2023**, *6* (1), 65. https://doi.org/10.1038/s41612-023-00393-4
(28) Zhang, J.; Jin, L.; Xu, X.; Neyestani, S. E.; Zhang, X.; Ho, T.; Zhang, J.; Butler, J.; Preble, C. V.; Kirchstetter, T. W.; Ying, Q.; Chen, Z.; Spurlock, A.; Breunig, H. Source-Resolved Inversion of Elemental Carbon Emissions in California Using Log-Space Bayesian Inference. *ACS EST Air* **2026**. https://doi.org/10.1021/acsestair.6c00105
(29) *Chemical Speciation Network (CSN) Annual Quality Report*; Air Quality Research Center, University of California, Davis, 2025.
(30) *Interagency Monitoring of Protected Visual Enviroments (IMPROVE) Annual Quality Assurance Report*; Air Quality Research Center, University of California, Davis, 2025.
(31) Norris, G.; Duvall, R.; Brown, S.; Bai, S. Positive Matrix Factorization (PMF) 5.0 Fundamentals and User Guide.
(32) Foroutan, H.; Young, J.; Napelenok, S.; Ran, L.; Appel, K. W.; Gilliam, R. C.; Pleim, J. E. Development and Evaluation of a Physics-Based Windblown Dust Emission Scheme Implemented in the CMAQ Modeling System. *Journal of Advances in Modeling Earth Systems* **2017**, *9* (1), 585–608. https://doi.org/10.1002/2016MS000823
(33) Gantt, B.; Kelly, J. T.; Bash, J. O. Updating Sea Spray Aerosol Emissions in the Community Multiscale Air Quality (CMAQ) Model Version 5.0.2. *Geoscientific Model Development* **2015**, *8* (11), 3733–3746. https://doi.org/10.5194/gmd-8-3733-2015
(34) Kelly, J. T.; Bhave, P. V.; Nolte, C. G.; Shankar, U.; Foley, K. M. Simulating Emission and Chemical Evolution of Coarse Sea-Salt Particles in the Community Multiscale Air Quality (CMAQ) Model. *Geoscientific Model Development* **2010**, *3* (1), 257–273. https://doi.org/10.5194/gmd-3-257-2010
(35) California Fire Incidents Database. https://www.fire.ca.gov/incidents
(36) Byun, D.; Schere, K. L. Review of the Governing Equations, Computational Algorithms, and Other Components of the Models-3 Community Multiscale Air Quality (CMAQ) Modeling System. *Appl. Mech. Rev* **2006**, *59* (2), 51–77. https://doi.org/10.1115/1.2128636
(37) Reff, A.; Bhave, P. V.; Simon, H.; Pace, T. G.; Pouliot, G. A.; Mobley, J. D.; Houyoux, M. Emissions Inventory of PM2.5 Trace Elements across the United States. *Environ. Sci. Technol.* **2009**, *43* (15), 5790–5796. https://doi.org/10.1021/es802930x
(38) Mastin, J.; Saini, A.; Schuster, J. K.; Harner, T.; Dabek-Zlotorzynska, E.; Celo, V.; Gaga, E. O. Trace Metals in Global Air: First Results from the GAPS and GAPS Megacities Networks. *Environ. Sci. Technol.* **2023**, *57* (39), 14661–14673. https://doi.org/10.1021/acs.est.3c05733
(39) Liao, K.; Park, E. S.; Zhang, J.; Cheng, L.; Ji, D.; Ying, Q.; Yu, J. Z. A Multiple Linear Regression Model with Multiplicative Log-Normal Error Term for Atmospheric Concentration Data. *Science of The Total Environment* **2021**, *767*, 144282. https://doi.org/10.1016/j.scitotenv.2020.144282
(40) *Risk-Screening Environmental Indicators Methodology Document, Version 2.3.12*. https://www.epa.gov/system/files/documents/2024-03/rsei-methodology-document-v2312-march2024.pdf (accessed 2026-07-04)

(41) *TIGER/Line® Shapefiles*. https://www.census.gov/cgi-bin/geo/shapefiles/index.php (accessed 2026-09-07)
(42) Sun, J.; Shen, Z.; Zhang, L.; Lei, Y.; Gong, X.; Zhang, Q.; Zhang, T.; Xu, H.; Cui, S.; Wang, Q.; Cao, J.; Tao, J.; Zhang, N.; Zhang, R. Chemical Source Profiles of Urban Fugitive Dust PM2.5 Samples from 21 Cities across China. *Science of The Total Environment* **2019**, *649*, 1045–1053. https://doi.org/10.1016/j.scitotenv.2018.08.374
(43) Zieger, P.; Väisänen, O.; Corbin, J. C.; Partridge, D. G.; Bastelberger, S.; Mousavi-Fard, M.; Rosati, B.; Gysel, M.; Krieger, U. K.; Leck, C.; Nenes, A.; Riipinen, I.; Virtanen, A.; Salter, M. E. Revising the Hygroscopicity of Inorganic Sea Salt Particles. *Nat Commun* **2017**, *8* (1), 15883. https://doi.org/10.1038/ncomms15883
(44) Jayarathne, T.; Sultana, C. M.; Lee, C.; Malfatti, F.; Cox, J. L.; Pendergraft, M. A.; Moore, K. A.; Azam, F.; Tivanski, A. V.; Cappa, C. D.; Bertram, T. H.; Grassian, V. H.; Prather, K. A.; Stone, E. A. Enrichment of Saccharides and Divalent Cations in Sea Spray Aerosol During Two Phytoplankton Blooms. *Environ. Sci. Technol.* **2016**, *50* (21), 11511–11520. https://doi.org/10.1021/acs.est.6b02988
(45) England, G. C.; Watson, J. G.; Chow, J. C.; Zielinska, B.; Chang, M.-C. O.; Loos, K. R.; Hidy, G. M. Dilution-Based Emissions Sampling from Stationary Sources: Part 2—Gas-Fired Combustors Compared with Other Fuel-Fired Systems. *Journal of the Air & Waste Management Association* **2007**, *57* (1), 79–93. https://doi.org/10.1080/10473289.2007.10465304
(46) Zheng, L.; Wu, D.; Chen, X.; Li, Y.; Cheng, A.; Yi, J.; Li, Q. Chemical Profiles of Particulate Matter Emitted from Anthropogenic Sources in Selected Regions of China. *Sci Data* **2024**, *11* (1), 1206. https://doi.org/10.1038/s41597-024-04058-6
(47) Zeng, X.; Kong, S.; Zhang, Q.; Ren, H.; Liu, J.; Feng, Y.; Yan, Q.; Qin, S.; Zheng, S.; Yao, L.; Fan, Z.; Zhang, Y.; Liu, X.; Yan, Y.; Zhu, K.; Ding, F.; Liu, W.; Liu, D.; Qi, S.; Fu, P. Source Profiles and Emission Factors of Organic and Inorganic Species in Fine Particles Emitted from the Ultra-Low Emission Power Plant and Typical Industries. *Science of The Total Environment* **2021**, *789*, 147966. https://doi.org/10.1016/j.scitotenv.2021.147966
(48) Sha, Q.; Lu, M.; Huang, Z.; Yuan, Z.; Jia, G.; Xiao, X.; Wu, Y.; Zhang, Z.; Li, C.; Zhong, Z.; Zheng, J. Anthropogenic Atmospheric Toxic Metals Emission Inventory and Its Spatial Characteristics in Guangdong Province, China. *Science of The Total Environment* **2019**, *670*, 1146–1158. https://doi.org/10.1016/j.scitotenv.2019.03.206
(49) Ihantola, T.; Di Bucchianico, S.; Happo, M.; Ihalainen, M.; Uski, O.; Bauer, S.; Kuuspalo, K.; Sippula, O.; Tissari, J.; Oeder, S.; Hartikainen, A.; Rönkkö, T. J.; Martikainen, M.-V.; Huttunen, K.; Vartiainen, P.; Suhonen, H.; Kortelainen, M.; Lamberg, H.; Leskinen, A.; Sklorz, M.; Michalke, B.; Dilger, M.; Weiss, C.; Dittmar, G.; Beckers, J.; Irmler, M.; Buters, J.; Candeias, J.; Czech, H.; Yli-Pirilä, P.; Abbaszade, G.; Jakobi, G.; Orasche, J.; Schnelle-Kreis, J.; Kanashova, T.; Karg, E.; Streibel, T.; Passig, J.; Hakkarainen, H.; Jokiniemi, J.; Zimmermann, R.; Hirvonen, M.-R.; Jalava, P. I. Influence of Wood Species on Toxicity of Log-Wood Stove Combustion Aerosols: A Parallel Animal and Air-Liquid Interface Cell Exposure Study on Spruce and Pine Smoke. *Part Fibre Toxicol* **2020**, *17* (1), 27. https://doi.org/10.1186/s12989-020-00355-1
(50) Liu, Y.; Zhang, W.; Yang, W.; Bai, Z.; Zhao, X. Chemical Compositions of PM2.5 Emitted from Diesel Trucks and Construction Equipment. *Aerosol Sci Eng* **2018**, *2* (2), 51–60. https://doi.org/10.1007/s41810-017-0020-2

(51) Wang, M.; Wang, Z.; Wang, Y.; Shi, Z.; Peng, B.; Zhang, F.; Wang, G.; Yang, Y. Stagnant Oxidative Potential in Declining Agricultural Fleets: Evidence from Key Particulate Matter Composition despite Fleet Renewal. *Eco-Environment & Health* **2026**, *5* (2), 100230. https://doi.org/10.1016/j.eehl.2026.100230
(52) Cui, M.; Chen, Y.; Feng, Y.; Li, C.; Zheng, J.; Tian, C.; Yan, C.; Zheng, M. Measurement of PM and Its Chemical Composition in Real-World Emissions from Non-Road and on-Road Diesel Vehicles. *Atmospheric Chemistry and Physics* **2017**, *17* (11), 6779–6795. https://doi.org/10.5194/acp-17-6779-2017
(53) Corbin, J. C.; Mensah, A. A.; Pieber, S. M.; Orasche, J.; Michalke, B.; Zanatta, M.; Czech, H.; Massabò, D.; Buatier de Mongeot, F.; Mennucci, C.; El Haddad, I.; Kumar, N. K.; Stengel, B.; Huang, Y.; Zimmermann, R.; Prévôt, A. S. H.; Gysel, M. Trace Metals in Soot and PM2.5 from Heavy-Fuel-Oil Combustion in a Marine Engine. *Environ. Sci. Technol.* **2018**, *52* (11), 6714–6722. https://doi.org/10.1021/acs.est.8b01764
(54) Griffith, J. D. Electron Microscopic Characterization of Exhaust Particles Containing Lead Dibromide Beads Expelled from Aircraft Burning Leaded Gasoline. *Atmospheric Pollution Research* **2020**, *11* (9), 1481–1486. https://doi.org/10.1016/j.apr.2020.05.026
(55) Schauer, J. J.; Lough, G. C.; Shafer, M. M.; Christensen, W. F.; Arndt, M. F.; DeMinter, J. T.; Park, J.-S. *Characterization of Metals Emitted from Motor Vehicles*; Research Report; Health Effects Institute: Boston, MA, 2006. https://www.healtheffects.org/publication/characterization-metals-emitted-motor-vehicles
(56) Yang, H.-H.; Dhital, N. B.; Wang, L.-C.; Hsieh, Y.-S.; Lee, K.-T.; Hsu, Y.-T.; Huang, S.-C. Chemical Characterization of Fine Particulate Matter in Gasoline and Diesel Vehicle Exhaust. *Aerosol Air Qual. Res.* **2019**, *19* (6), 1349–1449. https://doi.org/10.4209/aaqr.2019.04.0191
(57) Parkin, J. G. H.; Dean, L. S. N.; Bell, J. A.; Easton, N. H. C.; Edgeway, L. J.; Cooper, M. J.; Ridley, R.; Conforti, F.; Wang, S.; Yao, L.; Li, J.; Raj, H. V.; Downward, J.; Gerlofs-Nijland, M.; Cassee, F. R.; Wang, Y.; Cook, R. B.; Jones, M. G.; Davies, D. E.; Loxham, M. Copper-Enriched Automotive Brake Wear Particles Perturb Human Alveolar Cellular Homeostasis. *Part Fibre Toxicol* **2025**, *22* (1), 4. https://doi.org/10.1186/s12989-024-00617-2
(58) Vaziri, N. D. Mechanisms of Lead-Induced Hypertension and Cardiovascular Disease. *American Journal of Physiology-Heart and Circulatory Physiology* **2008**, *295* (2), H454–H465. https://doi.org/10.1152/ajpheart.00158.2008
(59) Charrier, J. G.; McFall, A. S.; Richards-Henderson, N. K.; Anastasio, C. Hydrogen Peroxide Formation in a Surrogate Lung Fluid by Transition Metals and Quinones Present in Particulate Matter. *Environ. Sci. Technol.* **2014**, *48* (12), 7010–7017. https://doi.org/10.1021/es501011w
(60) Kehrer, J. P. The Haber–Weiss Reaction and Mechanisms of Toxicity. *Toxicology* **2000**, *149* (1), 43–50. https://doi.org/10.1016/S0300-483X(00)00231-6
(61) Particulate Matter Air Pollution and Cardiovascular Disease. *Circulation*.
(62) Men, Z.-Y.; Liu, D.-Y.; Guo, Q.-Y.; Zhang, J.; Peng, J.-F.; Wu, L.; Mao, H.-J. [Chemical Component of Particulate Matters and VOCs Characteristics During Vehicle Brake Processes]. *Huan Jing Ke Xue* **2022**, *43* (10), 4348–4356. https://doi.org/10.13227/j.hjkx.202112127

(63) U.S. Department of Agriculture Economic Research Service. 2010 Rural-Urban Commuting Area Codes, 2019. https://www.ers.usda.gov/data-products/rural-urban-commuting-area-codes (accessed 2026-09-21)
(64) Galon-Negru, A. G.; Olariu, R. I.; Arsene, C. Size-Resolved Measurements of PM2.5 Water-Soluble Elements in Iasi, North-Eastern Romania: Seasonality, Source Apportionment and Potential Implications for Human Health. *Science of The Total Environment* **2019**, *695*, 133839. https://doi.org/10.1016/j.scitotenv.2019.133839
(65) Tehrani, M. W.; Fortner, E. C.; Robinson, E. S.; Chiger, A. A.; Sheu, R.; Werden, B. S.; Gigot, C.; Yacovitch, T.; Van Bramer, S.; Burke, T.; Koehler, K.; Nachman, K. E.; Rule, A. M.; DeCarlo, P. F. Characterizing Metals in Particulate Pollution in Communities at the Fenceline of Heavy Industry: Combining Mobile Monitoring and Size-Resolved Filter Measurements. *Environ. Sci.: Processes Impacts* **2023**, *25* (9), 1491–1504. https://doi.org/10.1039/d3em00142c
(66) U.S. Environmental Protection Agency. *Methods to Develop Inhalation Cancer Risk Estimates for Chromium and Nickel Compounds*; U.S. Environmental Protection Agency, Office of Air Quality Planning and Standards: Research Triangle Park, NC, 2011. https://nepis.epa.gov/Exe/ZyPURL.cgi?Dockey=P100DE38.TXT
(67) U.S. Environmental Protection Agency. *EPA's Risk-Screening Environmental Indicators (RSEI) Methodology*, RSEI Version 2.3.12.; U.S. Environmental Protection Agency, Office of Pollution Prevention and Toxics: Washington, DC, 2024. https://www.epa.gov/system/files/documents/2024-03/rsei-methodology-document-v2312-march2024.pdf
(68) U.S. Environmental Protection Agency. *Air Toxic Emissions from Onroad Vehicles in MOVES3*; U.S. Environmental Protection Agency, Office of Transportation and Air Quality, 2020. https://nepis.epa.gov/Exe/ZyPURL.cgi?Dockey=P1010TJM.TXT
(69) California Air Resources Board; Office of Environmental Health Hazard Assessment. *Study of Neighborhood Air near Petroleum Sources (SNAPS): Lost Hills, California. Final Report*; California Air Resources Board and Office of Environmental Health Hazard Assessment: Sacramento, CA, 2025. https://ww2.arb.ca.gov/sites/default/files/2025-10/SNAPS_Lost_Hills_Final_Report.pdf
(70) Łożyńska, M.; Trojanowska, M.; Molik, A.; Świetlik, R. Measurement Report: Seasonal Trends and Chemical Speciation of Chromium(III/VI) in Different Fractions of Urban Particulate Matter – a Case Study of Radom, Poland. *Atmospheric Chemistry and Physics* **2025**, *25* (18), 10499–10510. https://doi.org/10.5194/acp-25-10499-2025
(71) South Coast Air Quality Management District. *AB 2588 Public Notification*. South Coast AQMD. https://www.aqmd.gov/nav/about/public-notices/ab-2588-notices (accessed 2026-09-21)